Efficient Radar Target Classification Using Adaptive Joint Time-Frequency Processing

Kyung-Tae Kim, In-Sik Choi, and Hyo-Tae Kim

***Abstract*—This paper presents a new target recognition scheme via adaptive Gaussian representation, which uses adaptive joint time-frequency processing techniques. The feature extraction stage of the proposed scheme utilizes the geometrical moments of the adaptive spectrogram. For this purpose, we have derived exact and closed form expressions of geometrical moments of the adaptive spectrogram in the time, frequency, and joint time-frequency domains. Features obtained by this method can provide substantial savings of computational resources, preserving as much essential information for classifying targets as possible. Next, a principal component analysis is used to further reduce the dimension of feature space, and the resulting feature vectors are passed to the classifier stage based on the multilayer perceptron neural network. To demonstrate the performance of the proposed scheme, various thin-wire targets are identified. The results show that the proposed technique has a significant potential for use in target recognition.**

I. Introduction

TARGET recognition problems from the backscattered fields of radar targets have long been very difficult to solve because scattering mechanisms are very complicated, even for a geometrically simple target, and also because they have strong frequency and angle dependencies. Therefore, it is necessary to represent these complex scattering mechanisms in an efficient manner. Consequently, inverse synthetic aperture radar (ISAR) images and complex natural resonance (CNR) frequencies have been utilized for this purpose.

An ISAR image, which is a type of time-domain representation of a backscattered field for a target, can display the two-dimensional (2-D) spatial distribution of nondispersive scattering centers in a 2-D image plane [1], and they have been used as features for target recognition [2]. Unlike ISAR images, CNR frequencies from the late-time portion of the backscattered signal are a kind of frequency-domain representation, which have also been applied to radar target recognition in conjunction with E-pulse, S-pulse, and generalized likelihood ratio test (GLRT) techniques [3]–[5]. On the other hand, time-frequency (T-F) analysis has many advantages over conventional ISAR images and CNR frequencies, since it can display both time-domain scattering phenomena, like scattering centers, and frequency-domain scattering phenomena, such as local resonances and dispersive mechanisms, in a 2-D T-F axis. This can lead to more abundant scattering information about a target than that from either time or frequency domain representation alone, and therefore the T-F features are very useful for target recognition applications.

T-F analysis techniques have long been used in the area of diagnostic investigation to reveal the complicated scattering mechanisms of certain structures such as an open-ended circular waveguide cavity, uniform plasma cylinder, and slotted waveguide, etc. [6]–[8]. In these studies, the short-time Fourier transform (STFT), Wigner–Ville distribution (WVD), and wavelet transform have been employed as main signal processing tools for investigating target diagnostics. However, recently developed adaptive joint T-F processing techniques, such as adaptive Gaussian representation (AGR), adaptive chirplet-based signal approximation, and a matching pursuit algorithm [9]–[11] have many advantages over the conventional T-F processing methods mentioned above. In contrast to the conventional nonparametric T-F analysis such as STFT, WVD, and wavelet transform, the adaptive joint T-F processing technique is a type of parametric T-F analysis, and therefore it can provide very high T-F resolution. Moreover, since AGR can decompose the backscattered signal into T-F centers corresponding to scattering centers and local resonances, it has been used in the application of ISAR image enhancement and data compression [12], [13]. Also, the adaptive chirplet-based signal approximation has been applied to ISAR motion compensation [14].

In terms of target recognition, it has been found that T-F signatures from a target change in a well-behaved manner with the aspect angles throughout the entire angular range of the target. This suggests that the identification of complex-shaped targets can be based upon a small set of templates for each given target [15]. The most critical issue when using T-F features for target recognition is the prohibitive memory space problem for the construction of a database containing T-F signatures with the change of target type and aspect angle. Therefore, what is most important is to reduce the dimension of the T-F signature while preserving as much essential information as possible.

In this paper, we propose a new target-recognition strategy based on AGR processing. AGR assumes that the backscattered field from a target consists of adaptive normalized Gaussian basis functions with adjustable T-F centers and associated variances. These elementary Gaussian modes contained in the backscattered signal can be found by the iterative procedure described in [9]. With these extracted T-F centers of Gaussian modes, the geometrical moments of the adaptive spectrogram (ADS) are computed using the derived expressions in this paper without time-consuming ADS generation. The small

Manuscript received July 14, 1999; revised April 12, 2000. This work was supported by the Korean Agency for Defense Development under Contract EM-44 and the Ministry of Education of Korea by supporting the Electrical and Computer Engineering Division of POSTECH through its BK21 program.

The authors are with the Electrical and Computer Engineering Division, Pohang University of Science and Technology, Kyungpook 790-784, Korea.

Publisher Item Identifier S 0018-926X(00)07716-4.

dimensional geometrical moments obtained are further transformed into feature vectors of much smaller dimension via the use of principal component analysis (PCA). Next, the feature vectors finally obtained from several targets are identified using a classifier based on the multilayer perceptron neural network. Classification results using several thin-wire targets will demonstrate the effectiveness of the proposed procedure.

II. AGR Theory

AGR expands a backscattered field in time-domain $r(t)$ in terms of normalized Gaussian elementary functions $h_p(t)$ with an adjustable T-F center (t_p, f_p) and a variance α_p

$$r(t) = \sum_{p=0}^{\infty} B_p h_p(t) \tag{1}$$

where

$$h_p(t) = (\pi\alpha_p)^{-0.25} \exp\left[-\frac{(t-t_p)^2}{2\alpha_p}\right] \exp(j2\pi f_p t).$$

The adjustable parameters t_p, f_p, and α_p for Gaussian basis functions, and B_p for the coefficient can be obtained such that $h_p(t)$ is most similar to $r_p(t)$

$$|B_p|^2 = \max_{t_p,\, f_p,\, \alpha_p} \left| \int r_p(t) h_p^*(t)\, dt \right|^2, \quad \alpha_p \in \mathbf{R}^+,\ t_p,\ f_p \in \mathbf{R} \tag{2}$$

where $r_0(t) = r(t)$. $r_{p+1}(t)$ is the remainder after the orthogonal projection of $r_p(t)$ onto $h_p(t)$ and this iterative procedure is described as

$$r_{p+1}(t) = r_p(t) - B_p h_p(t). \tag{3}$$

Since the projection integral in (2) is the Fourier transform of $r_p(t)$ with the Gaussian window, $w(t) = (\pi\alpha_p)^{-0.25} \exp[-((t - t_p)^2/2\alpha_p)]$, the adjustable T-F center (t_p, f_p) and associated variance α_p can be obtained using the computationally efficient fast Fourier transform (FFT) and the specific search procedure in [9]. That is, beginning with large scale (variance) α_p, which determines the time and frequency widths of a Gaussian basis function, the T-F center having the maximum B_p is selected. Then, the scale α_p is halved and another T-F center of the maximum B_p is found. This process continues until the maximum B_p no longer increases. The t_p, f_p, α_p, and B_p finally obtained give the solution of (2) and these four parameters completely describe one Gaussian T-F basis function at the pth iteration. A detailed graphical illustration of this search procedure in the T-F domain can be found in [12].

In the actual implementation of the above AGR algorithm, the upper limit of the summation in (1) is limited to $p_{\max}$ since the iteration halts after the extracted Gaussian basis functions faithfully approximate the time-domain signal $r(t)$ with sufficiently high accuracy. After $p_{\max}$ stages of AGR decomposition, the following relationships hold:

$$r(t) = \sum_{p=0}^{p_{\max}} B_p h_p(t) + r_{p_{\max}+1}(t) \tag{4}$$

and

$$\|r(t)\|^2 = \sum_{p=0}^{p_{\max}} |B_p|^2 + \|r_{p_{\max}+1}(t)\|^2. \tag{5}$$

Therefore, the AGR iteration in (3) continues until the reconstruction error $\|r_{p_{\max}+1}(t)\|^2$ is sufficiently small, i.e., $\gamma = ((\sum_{p=0}^{p_{\max}} |B_p|^2)/\|r(t)\|^2)(<1)$, the ratio between the energy of the reconstructed signal $\sum_{p=0}^{p_{\max}} |B_p|^2$ and the energy of the original signal $\|r(t)\|^2$, is close to unity and, hence, the upper limit $p_{\max}$ is determined [9].

After t_p, f_p, α_p, and B_p, $p = 0, 1, 2, \ldots, p_{\max}$ are obtained via AGR processing, the ADS, which is a signal energy distribution in the joint T-F plane, $s(t, f)$ is given by

$$s(t, f) = \sum_{p=0}^{p_{\max}} 2|B_p|^2 \times \exp\left[-\frac{(t-t_p)^2}{\alpha_p} - (2\pi)^2 \alpha_p (f - f_p)^2\right]. \tag{6}$$

It is well known that this ADS can give a joint T-F distribution that is nonnegative, cross-term interference free, and of high resolution [9].

Note that the Gaussian elementary functions used in (1) does not constitute a complete set (orthonormal basis), while those of the wavelet decomposition and the modified Gabor expansion developed by Bastiaans form a complete set [16], [17]. Unless the elementary functions form a complete set, such representation may be redundant and its uniqueness may not be guaranteed. However, the time and frequency resolutions of the elementary functions in both the wavelet decomposition and Bastiaans' method are restricted to a regular sampling grid [9], and in addition, they are subject to the number of data samples [18]. In radar signal processing applications, the scattering mechanisms are usually too complicated, and consequently, for accurate representation of a radar signature, it is desirable to have the elementary functions on a flexible sampling grid as in AGR processing rather than the elementary functions on a regular grid as in the two methods mentioned above. The effectiveness of AGR processing for radar applications has been well discussed in [13] and [19].

III. Feature Extraction from Adaptive Spectrogram

In order to apply the T-F distribution for radar target recognition, attention should be focused on the reduction of the feature space dimension. Because the T-F distribution itself is a 2-D image in the T-F plane, a large amount of memory storage is required to store recognition features for many target classes and aspect angles. In terms of visual pattern recognition, the moments invariants derived from the geometrical moments of a 2-D image have been utilized to reduce the dimension of the 2-D image feature [20], [21] since they have small dimensions and are invariant features under translation, scale, and rotation.

In this paper, the geometrical moments of the T-F distribution are directly used as features for target recognition.

Given a 2-D density distribution function $f(x, y)$, the 2-D geometrical moments of qth order in the x-domain, those of rth order in the y-domain, and those of $(q+r)$th order in the xy-domain are defined as follows [20]:

$$m_q^{x,2} = \int_{-\infty}^{\infty}\int_{-\infty}^{\infty} x^q f(x, y)\,dx\,dy, \quad q = 0, 1, 2, \ldots \tag{7}$$

$$m_r^{y,2} = \int_{-\infty}^{\infty}\int_{-\infty}^{\infty} y^r f(x, y)\,dx\,dy, \quad r = 0, 1, 2, \ldots \tag{8}$$

$$m_{qr}^{xy,2} = \int_{-\infty}^{\infty}\int_{-\infty}^{\infty} x^q y^r f(x, y)\,dx\,dy, \quad q, r = 0, 1, 2, \ldots. \tag{9}$$

If $f(x, y)$ is assumed to be a piecewise continuous and bounded function, the moments sequences, $m_q^{x,2}$, $m_r^{y,2}$, and $m_{qr}^{xy,2}$ are uniquely determined by $f(x, y)$ and conversely, $f(x, y)$ are uniquely determined by $m_q^{x,2}$, $m_r^{y,2}$, and $m_{qr}^{xy,2}$.

For a 2-D $M \times N$ image $f(x_i, y_j)$, $(i = 1, 2, \ldots, M, j = 1, 2, \ldots, N)$, (7)–(9) can be approximated as [2], [22]

$$m_q^{x,2} \approx \sum_{i=1}^{M}\sum_{j=1}^{N} x_i^q f(x_i, y_j), \quad q = 0, 1, 2, \ldots \tag{10}$$

$$m_r^{y,2} \approx \sum_{i=1}^{M}\sum_{j=1}^{N} y_j^r f(x_i, y_j), \quad r = 0, 1, 2, \ldots \tag{11}$$

$$m_{qr}^{xy,2} \approx \sum_{i=1}^{M}\sum_{j=1}^{N} x_i^q y_j^r f(x_i, y_j), \quad q, r = 0, 1, 2, \ldots. \tag{12}$$

It is noted that $m_q^{x,2}$, $m_r^{y,2}$, and $m_{qr}^{xy,2}$ in (10)–(12) can provide geometrical moments of an $M \times N$ image only in an approximate sense. That is, if the geometrical moments of an image are obtained using (10)–(12), the accuracy of the estimated values is dependent on the image size $M \times N$, i.e., resolution of the given image. If the resolution of an image is low, the accuracy decreases, and vice versa.

To overcome this limitation in the computation of 2-D geometrical moments for ADS, we first define the time- and frequency-domain standard deviations, $\sigma_{tp} = \sqrt{\alpha_p/2}$ and $\sigma_{fp} = 1/(2\pi\sqrt{2\alpha_p})$, respectively. Then the ADS in (6) becomes

$$s(t, f) = \sum_{p=0}^{p_{\max}} 4\pi\sigma_{tp}\sigma_{fp}|B_p|^2 g_{tp}(t) g_{fp}(f) \tag{13}$$

where

$$g_{tp}(t) = \frac{1}{\sigma_{tp}\sqrt{2\pi}}\exp\left[-\frac{(t-t_p)^2}{2\sigma_{tp}^2}\right], \quad \int_{-\infty}^{\infty} g_{tp}(t)\,dt = 1$$

$$g_{fp}(f) = \frac{1}{\sigma_{fp}\sqrt{2\pi}}\exp\left[-\frac{(f-f_p)^2}{2\sigma_{fp}^2}\right], \quad \int_{-\infty}^{\infty} g_{fp}(f)\,df = 1.$$

Note that each of $g_{tp}(t)$ and $g_{fp}(f)$ is in the form of a 1-D Gaussian probability density function with $t \sim \mathcal{N}(t_p, \sigma_{tp})$ and $f \sim \mathcal{N}(f_p, \sigma_{fp})$, respectively.

Combining (6), (7), and (13), the 2-D time-domain geometrical moments of qth-order $m_q^{t,2}$ for ADS can be expressed as

$$\begin{aligned} m_q^{t,2} &= \int_{-\infty}^{\infty}\int_{-\infty}^{\infty} t^q s(t, f)\,dt\,df \\ &= \sum_{p=0}^{p_{\max}} 4\pi\sigma_{tp}\sigma_{fp}|B_p|^2 \int_{-\infty}^{\infty}\int_{-\infty}^{\infty} t^q g_{tp}(t) g_{fp}(f)\,dt\,df \\ &= \sum_{p=0}^{p_{\max}} 4\pi\sigma_{tp}\sigma_{fp}|B_p|^2 \int_{-\infty}^{\infty} t^q g_{tp}(t)\,dt \\ &= \sum_{p=0}^{p_{\max}} 4\pi\sigma_{tp}\sigma_{fp}|B_p|^2 \int_{-\infty}^{\infty} t^q \frac{1}{\sigma_{tp}\sqrt{2\pi}} \\ &\quad \times \exp\left[-\frac{(t-t_p)^2}{2\sigma_{tp}^2}\right] dt \\ &= \sum_{p=0}^{p_{\max}} 4\pi\sigma_{tp}\sigma_{fp}|B_p|^2 m_q^{t,1}, \quad q = 0, 1, 2, \ldots. \end{aligned} \tag{14}$$

In (14), $m_q^{t,1}$ are 1-D moments with $t \sim \mathcal{N}(t_p, \sigma_{tp})$. On the other hand, $m_q^{t,1}$ can be expanded in terms of 1-D kth-order central moments $\mu_k^{t,1}$ and its mean t_p as follows [23]:

$$m_q^{t,1} = E[t^q] = \sum_{k=0}^{q}\binom{q}{k}\mu_k^{t,1} t_p^{q-k} \tag{15}$$

where

$$\begin{aligned} \mu_k^{t,1} &= E\left[(t-t_p)^k\right] \\ &= \int_{-\infty}^{\infty}(t-t_p)^k \frac{1}{\sigma_{tp}\sqrt{2\pi}}\exp\left[-\frac{(t-t_p)^2}{2\sigma_{tp}^2}\right] dt \\ &= \int_{-\infty}^{\infty}\frac{1}{\sigma_{tp}\sqrt{2\pi}} z^k \exp\left(-\frac{z^2}{2\sigma_{tp}^2}\right) dz \\ &= \begin{cases} 0, & k = \text{odd} \\ (k-1)\sigma_{tp}^k, & k = \text{even}. \end{cases} \end{aligned} \tag{16}$$

Therefore, using (14)–(16), the exact and closed form of time-domain 2-D geometrical moments for ADS, $m_q^{t,2}$ are finally given by

$$m_q^{t,2} = \sum_{p=0}^{p_{\max}} 4\pi\sigma_{tp}\sigma_{fp}|B_p|^2 \sum_{\substack{k=0 \\ \text{even}}}^{q}\binom{q}{k}(k-1)\sigma_{tp}^k t_p^{q-k}, \quad q = 0, 1, 2, \ldots. \tag{17}$$

Similarly, the 2-D geometrical moments of rth-order in the frequency-domain and those of $(q+r)$th-order in the joint T-F domain can be expressed as

$$m_r^{f,2} = \sum_{p=0}^{p_{\max}} 4\pi\sigma_{tp}\sigma_{fp}|B_p|^2 \sum_{\substack{k=0 \\ \text{even}}}^{r}\binom{r}{k}(k-1)\sigma_{fp}^k f_p^{r-k}, \quad r = 0, 1, 2, \ldots \tag{18}$$

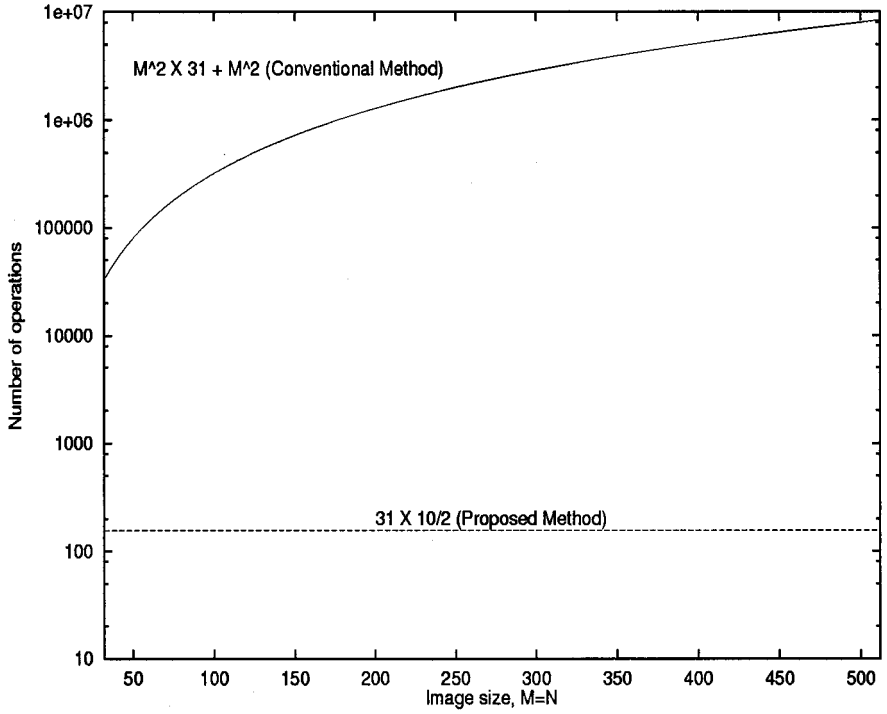

Fig. 1. Comparison of the number of operations needed to compute a time-domain geometrical moment between the conventional method and proposed method.

$$m_{qr}^{tf,2} = \sum_{p=0}^{p_{\max}} 4\pi\sigma_{tp}\sigma_{fp}|B_p|^2 \times \left[\sum_{\substack{k=0 \\ \text{even}}}^{q} \binom{q}{k}(k-1)\sigma_{tp}^{k} t_p^{q-k}\right] \times \left[\sum_{\substack{k=0 \\ \text{even}}}^{r} \binom{r}{k}(k-1)\sigma_{fp}^{k} f_p^{r-k}\right] \quad q, r = 0, 1, 2, \ldots. \tag{19}$$

So far, the exact and closed forms of 2-D geometrical moments for ADS have been derived. This implies that the moments can be calculated by merely using t_p, f_p, α_p, and B_p, $p = 0, 1, 2, \ldots, p_{\max}$ without time-consuming ADS generation. According to (6), $[MN\times(p_{\max}+1)]$ operations are needed to generate an $M \times N$ ADS image. Moreover, if we follow the conventional moments computation procedure in (10), additional MN operations are required to provide a single geometrical moment in the time-domain. Therefore, when using the conventional method, all $[MN\times(p_{\max}+1)+MN]$ operations are necessary to compute a time-domain geometrical moment if the four parameters, t_p, f_p, α_p, and B_p, $p = 0, 1, 2, \ldots, p_{\max}$ are given after the AGR processing. However, if the proposed method in (17) is utilized, approximately $[(p_{\max}+1)\times(q/2)]$ operations are needed to provide a qth-order time-domain geometrical moment of ADS. The computational saving becomes more significant as the image size, $M \times N$, increases in order to increase the T-F resolution for the improvement of recognition accuracy. This is illustrated in Fig. 1 in the case of $p_{\max} = 30$, $q = 10$, and $M = N$. In addition, as previously described, the proposed schemes in (17)–(19) can provide accurate geometrical moments of ADS in comparison with those obtained by the conventional methods in (10)–(12). This improvement of accuracy is important because we showed that the accuracy of a feature vector greatly affects the overall classification performance in the target recognition system [24].

In [24], the hybrid techniques combining FFT-based CLEAN algorithm and model-based algorithm have been developed to obtain robust and accurate estimates of 1-D scattering centers on the target. The performance of the developed hybrid techniques has been verified through the three-target classification experiment, which employs three different feature extraction stages based on the 1-D TLS (total least squares)-Prony algorithm, the hybrid technique (Hybrid-1) combining the modified CLEAN and LS (least squares)-Prony, and another hybrid technique (Hybrid-2) combining the modified CLEAN and modified LS-Prony, respectively. Next, the radial basis function (RBF) network was utilized to classify the test features involving 1-D scattering centers obtained by the above three different feature extraction techniques. The results show that the feature extraction stage based on the Hybrid-2 is the most suitable for radar target recognition. This is because the estimated parameter accuracy of the modified LS-Prony is better than that of the LS-Prony, and robustness is guaranteed through the FFT-based CLEAN algorithm. This implies that both the accuracy and robustness of the extracted feature vectors have an important role in the design of target recognition system. As a result, the exact and close forms of geometrical moments in (17)–(19) have two distinct advantages over the conventional methods in (10)–(12) in terms of computational efficiency and accuracy, resulting in an efficient target recognition system.

Finally, the feature vector for target recognition can be formed by concatenating the obtained geometrical moments from the first and Lth-order as follows:

$$\begin{aligned}\mathbf{x} &= [x_1, x_2, x_3, \ldots, x_K]^T \\ &= \left[m_1^{t,2}, m_1^{f,2}, m_{11}^{tf,2}, m_2^{t,2}, m_2^{f,2}, m_{22}^{tf,2}, \ldots, \right. \\ &\qquad \left. m_L^{t,2}, m_L^{f,2}, m_{LL}^{tf,2}\right]^T \end{aligned} \tag{20}$$

where $K = 3L$. While other combinations of orders are possible to form a feature vector, many computer simulations suggest that they have nearly no effect on the final classification result as long as the maximum order L is sufficiently large.

IV. Feature Space Reduction via Principal Component Analysis (PCA)

In (20), the feature vector $\mathbf{x}$ for target recognition is obtained by combining the 2-D geometrical moments of ADS, and its dimensionality is reasonably small if the maximum order L is not too large. In general, the geometrical moments of a 2-D complex image such as an optical photograph contain useful information up to a high order of magnitude. However, in the case of 2-D T-F image, the amount of information contained in its image plane is much smaller than that of an optical photograph. For example, the scattering center response of a target would be displayed as a vertical line parallel to the frequency axis in a T-F plane, and resonance response as a horizontal line parallel to the time axis. Of course, dispersive scattering mechanisms from cavities or duct-type structures would be seen as inclined lines in a T-F plane. Therefore, the essential information included in a T-F image plane can be represented by geometrical moments of relatively low orders. It is known from many computer simulations that the selection of L less than 10 shows sufficient classification accuracy, and the increase of L larger than 10 adds computational burden to the classifier without improving classification accuracy.

Usually, the geometrical moments in $\mathbf{x}$ contain redundant information and this redundancy can be effectively decreased by applying a decorrelation transform known as principal component analysis (PCA) [25]. After the application of PCA to the feature vectors in (20), the dimensionality of the original feature space, i.e., $K = 3L$, can be substantially reduced and the transformed feature vector in the new feature space has nearly no high-order components while still preserving low-order components.

Let N_c be the number of target classes and N_a be the number of aspect angles for the construction of a database, i.e., the training data set. Then, the overall training data set $\mathbf{X}$ has N_cN_a feature vectors of dimension K as follows:

$$\mathbf{X} = [\mathbf{x}_1, \mathbf{x}_2, \mathbf{x}_3, \ldots, \mathbf{x}_{N_cN_a}]^T \tag{21}$$

where

$$\mathbf{x}_i = i\text{th training feature vector.}$$

Then, the sample mean vector $\mathbf{m_x}$ and the sample covariance matrix $\mathbf{R_{xx}}$ can be given by

$$\mathbf{m_x} = \frac{1}{N_cN_a} \sum_{i=1}^{N_cN_a} \mathbf{x}_i \tag{22}$$

$$\mathbf{R_{xx}} = \frac{1}{N_cN_a - 1} \sum_{i=1}^{N_cN_a} (\mathbf{x}_i - \mathbf{m_x})(\mathbf{x}_i - \mathbf{m_x})^T. \tag{23}$$

The above $\mathbf{m_x}$ is a K-dimensional vector and $\mathbf{R_{xx}}$ is a $K \times K$ matrix.

Let the eigenvalues of the $\mathbf{R_{xx}}$ be denoted by $\lambda_1, \lambda_2, \ldots, \lambda_K$ $(\lambda_1 > \lambda_2 > \cdots > \lambda_K)$ and the associated eigenvectors be denoted by $\mathbf{q}_1, \mathbf{q}_2, \ldots, \mathbf{q}_K$. Then, matrix $\mathbf{R_{xx}}$ can be decomposed as follows:

$$\mathbf{R_{xx}} = \mathbf{Q}\mathbf{\Lambda}\mathbf{Q}^T \tag{24}$$

where

$$\begin{aligned}\mathbf{\Lambda} &= \text{diag}[\lambda_1, \lambda_2, \ldots, \lambda_K] \\ \mathbf{Q} &= [\mathbf{q}_1, \mathbf{q}_2, \ldots, \mathbf{q}_K].\end{aligned}$$

If we select the largest $l(<K)$ eigenvalues and associated eigenvectors of $\mathbf{R_{xx}}$, then the $K \times l$ transformation matrix $\mathbf{P}$ can be obtained by truncating $\mathbf{q}_{l+1}, \mathbf{q}_{l+2}, \ldots, \mathbf{q}_K$ of $\mathbf{Q}$. If the training data set has redundant information, l eigenvalues of $\mathbf{R_{xx}}$ are relatively large and the remaining $K-l$ eigenvalues are negligibly small. The number of largest eigenvalues l is dependent on the redundancy of the training data set. If the training data set has much redundant information, l increases, and vice versa. Since $K = 3L$ and L is the maximum order used in (20), the large value of L implies the training data set of high redundancy. In this paper, we have been always able to identify l value less than $(1/3)K$ for the case of $L = 10$, resulting in a compression factor larger than 3.

With the use of $\mathbf{P}$, we can reduce the feature space dimension from K to l without significant loss of information as follows:

$$\mathbf{y} = \mathbf{P}^T\mathbf{x} \tag{25}$$

where

$$\mathbf{P} = [\mathbf{q}_1, \mathbf{q}_2, \ldots, \mathbf{q}_l]$$

and $\mathbf{x}$ is a feature vector at an arbitrary aspect angle from any target class among N_c target classes. As a result, the resulting feature vector $\mathbf{y}$ has the dimension of l, and therefore, through the combined use of geometrical moments and PCA, the dimension of ADS, MN can be reduced to l, which is a very small value. For the computation of $\mathbf{P}$, the singular value decomposition (SVD) can be directly applied to the normalized training data matrix $\mathbf{X}' = [\mathbf{x}_1 - \mathbf{m_x}, \mathbf{x}_2 - \mathbf{m_x}, \mathbf{x}_3 - \mathbf{m_x}, \ldots, \mathbf{x}_{N_cN_a} - \mathbf{m_x}]$ instead of eigen-decomposition of $\mathbf{R_{xx}}$ since SVD has many computational advantages over eigen-decomposition in terms of computation accuracy and speed [25].

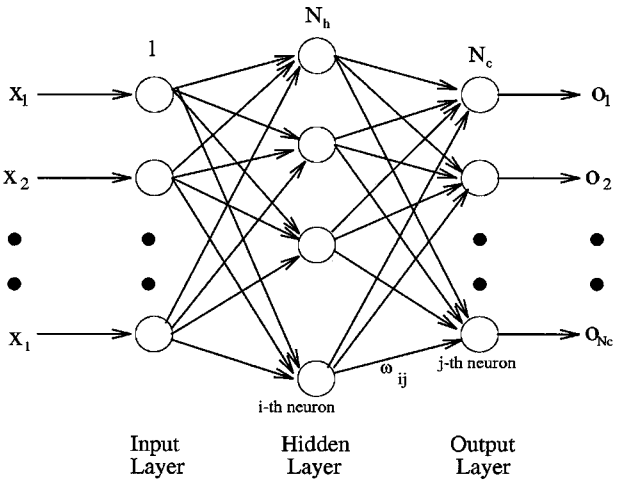

Fig. 2. The architecture of the MLPNN classifier.

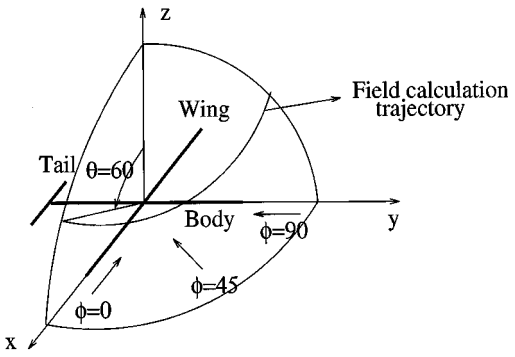

Fig. 3. Target geometry and backscattered field computation.

V. Multilayer Perceptron Neural Network Classifier

After N_cN_a training feature vectors $\mathbf{x}$ are transformed into $\mathbf{y}$ by PCA, we need to design a classifier to identify the target type. Although many classical pattern recognition algorithms are available for this purpose, neural networks are very promising due to their advantages over conventional pattern classification. The advantages of neural networks as pattern classifiers have been well investigated, and a detailed description of the architecture and training of neural networks can be found in [25]. The main reason for the feasibility of neural networks is their ability to generalize after learning from training data. That is, they can identify a test pattern even when that particular pattern is not used for training.

In this paper, a three-layer perceptron network, which is a kind of multilayer perceptron neural network (MLPNN), is used for designing a classifier. Fig. 2 shows a fully connected three-layer perceptron network with one hidden layer having N_h neurons. The number of neurons in the input layer is equal to the feature vector dimension l, and the number of neurons in the output layer is equal to the number of target classes N_c. The neurons in the MLPNN give a nonlinear transform between their inputs and outputs by the use of sigmoidal activation functions.

With the training data at N_a aspects for N_c target classes, the MLPNN in Fig. 2 is trained until its mean squared error (MSE) between the desired outputs and its actual outputs is less than a certain threshold level. The training strategy is based on the well-known back-propagation learning rule, which is an iterative algorithm updating each neuron's weight w_{ij} by searching the local gradient of the error surface. A detailed discussion for this MLPNN training algorithm can be found in [25]. After a sufficient number of training iterations using N_cN_a training patterns, a classifier having the ability to discriminate N_c target types can be formed, and it can identify a test feature vector at any aspect of any target among N_c targets. If a test feature vector $\mathbf{y}_{test}$ comes from the first target class, the above classifier will produce the largest output at the first neuron in the output layer.

In order to train the MLPNN to achieve the best classification accuracy, a large number of training iterations (i.e., a low MSE) are required in general. However, a simply low MSE value does not guarantee the best performance of the MLPNN. When the MLPNN is trained using too many training patterns, it may memorize the training data and therefore be less able to generalize test data, yielding degradation in classification performance [25]. To prevent the MLPNN from overtraining, the maximum number of iterations is usually defined to stop the training of the MLPNN. Therefore, the MLPNN should be stopped when the MSE is less than a certain threshold level, or the maximum number of iterations is reached.

VI. Classification Results

To demonstrate the performance of the proposed target recognition scheme, five targets in Fig. 3 and Table I are considered in this paper. All five targets are modeled as a combination of thin wires, and their physical dimensions are selected as 1/100 scale of the actual dimensions of the real aircrafts: Airbus, Boeing 747, Caravelle, P 7, and Tu 154. To obtain the radar return signals for these targets, the method of moments (MM) is used to calculate the backscattered fields in the frequency-domain. At an aspect of $\theta = 60°$ and $\phi = 45°$, the selected frequency range for backscattered field computation is $0 \sim 0.508$ GHz with a 4 MHz step, yielding 127 frequency points. This band covers the region of dominant resonant frequencies of the five targets. The frequency-domain backscattered field data for the five targets are converted into time-domain data by inverse FFT (IFFT). Then, after applying AGR processing to these time-domain data, the ADS results of the five targets are shown in Figs. 4–8. During AGR processing to estimate t_p, f_p, α_p, and B_p, the AGR iterations continue until the ratio $\gamma = ((\sum_{p=0}^{p_{\max}} |B_p|^2)/||r(t)||^2)$ reaches 0.9 for each target. Finally, five 127×127 ADS images, shown in Figs. 4–8, are produced using (6) and the estimated values for t_p, f_p, α_p, and B_p. Of course, the number of Gaussian modes $p_{\max}$ are different from one target to another.

By comparing Figs. 4–8, one can see that the general shapes of the T-F distributions for the five targets are similar. Although each figure shows both the specular reflections and resonances corresponding to each target, the differences between the resonance responses of the five targets are clearer than those of the specular returns. This is due to the fact that all five targets have the same geometries, but have different dimensions, resulting in different resonant frequencies. Note that the resonance responses are more important than specular returns in view of target recognition because they are aspect independent. With the

TABLE I
DIMENSIONS OF THE FIVE THIN WIRE TARGETS

Substructures	Target-1 (Airbus)	Target-2 (Boeing 747)	Target-3 (Caravelle)	Target-4 (P 7)	Target-5 (Tu 154)
Body span [m]	0.5408	0.7066	0.3200	0.3435	0.4790
Wing span [m]	0.4484	0.5964	0.3440	0.3250	0.3755
Tail span [m]	0.1626	0.2217	0.1092	0.1573	0.1340

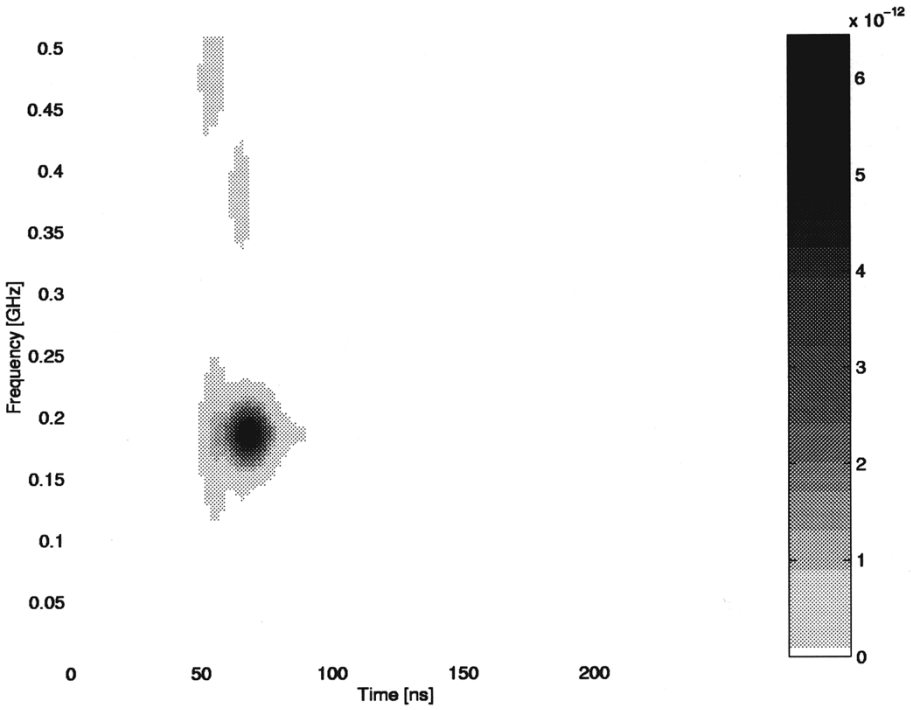

Fig. 4. ADS result of Target-1 (the AGR iteration continues until the γ exceeds at least 0.9, resulting in $p_{\max} = 20$).

proposed scheme, the ADS image is not computed since it requires too much memory storage and computation time.

An important parameter in any target recognition problem is the estimate of the correct classification rate P_c as a function of signal-to-noise ratio (SNR). To this end, some classification experiments have been carried out using the experimental setup in Fig. 9. As in the previous example, the backscattered fields of the five targets are computed using the MM in the frequency region of $0 \sim 0.508$ GHz with a 4 MHz step, but in this case the azimuth angle varies from $\phi = 0°$ to $\phi = 90°$ with $1°$ intervals at the fixed elevation angle of $\theta = 60°$, which is illustrated in Fig. 3. Therefore, 5 (number of target classes) $\times$ 91 (number of azimuth angle settings) $=$ 455 data files are generated for the experiment in Fig. 9.

To investigate the performance of the proposed technique in a noisy environment, an additive white Gaussian noise (AWGN) model is assumed and the desired SNR is achieved as follows:

$$z_i = s_i + \nu_i, \qquad i = 1, 2, \ldots, 127 \tag{26}$$

where z_i is the noise-corrupted data sequence, s_i is the original and complex data sequence in the frequency-domain, and ν_i is given by

$$\nu_i = \nu_i^R + j\nu_i^I, \qquad i = 1, 2, \ldots, 127 \tag{27}$$

where ν_i^R and ν_i^I are the white Gaussian noise sequences with zero mean values and each variance is equal to $\sigma_n^2/2$. σ_n^2 is the noise power needed to achieve the desired SNR[dB], and it is given by

$$\sigma_n^2 = P_s 10^{-(\mathrm{SNR[dB]}/10)} \tag{28}$$

where P_s is the power of the original data sequence s_i from any target at any azimuth angle.

To compute P_c, the available 455 data files must be divided into two sets: one for training and one for testing. In this experiment, the training data set is obtained by processing the data files from the even azimuth angles, $\phi = 0°, 2°, 4°, \ldots, 90°$. Thus, we have 5 (number of target classes) $\times$ 46 (number of even azimuth angle settings) $=$ 230 data files to design a classifier. After

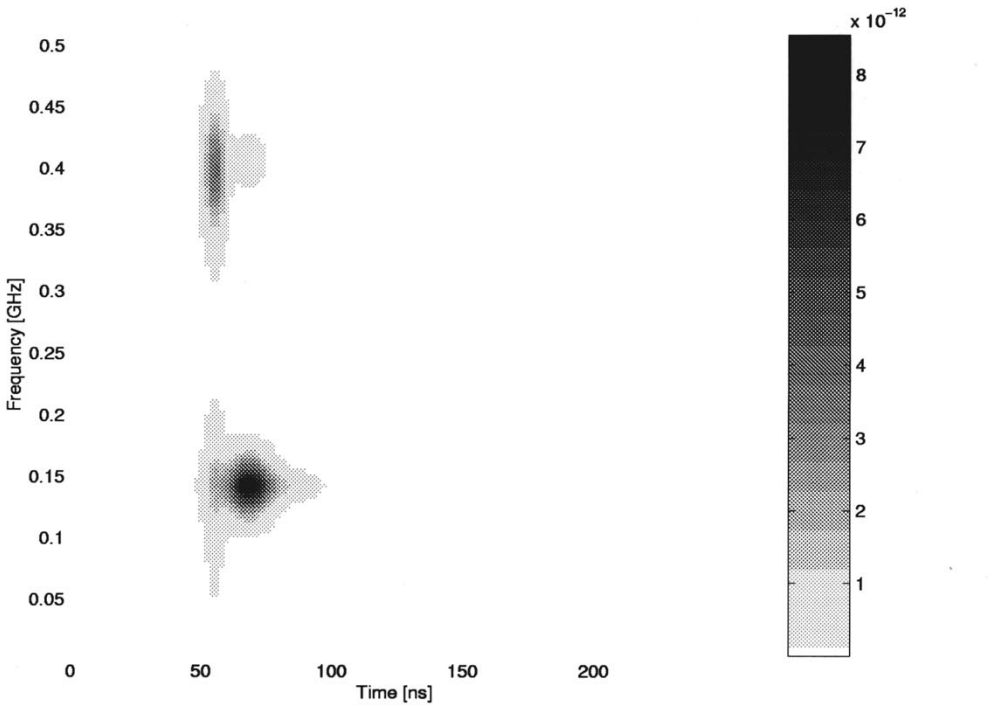

Fig. 5. ADS result of Target-2 (the AGR iteration continues until the γ exceeds at least 0.9, resulting in $p_{\max} = 16$).

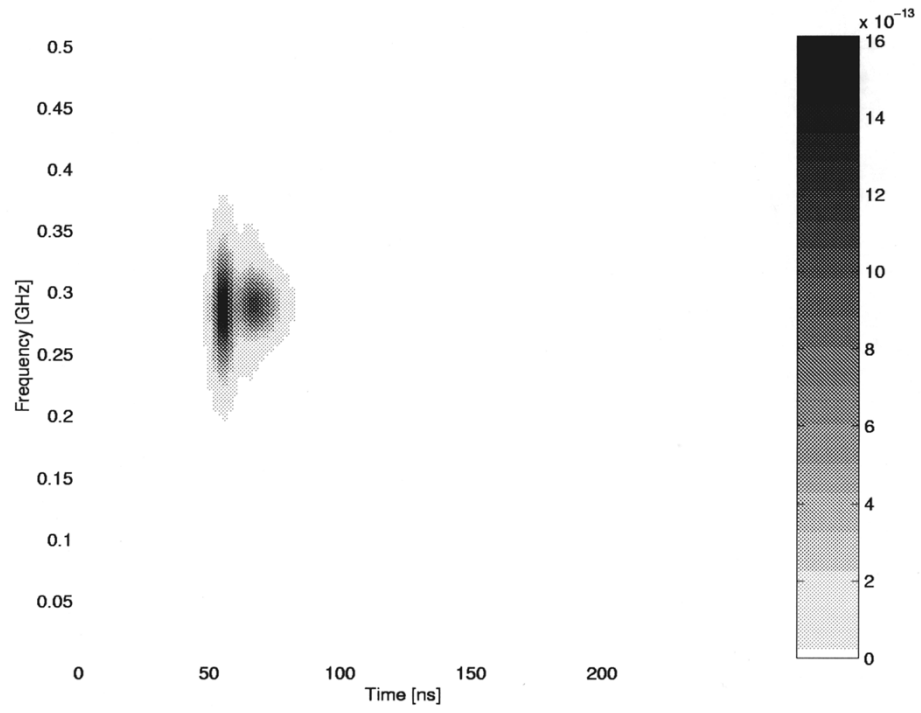

Fig. 6. ADS result of Target-3 (the AGR iteration continues until the γ exceeds at least 0.9, resulting in $p_{\max} = 11$).

the noise addition process in (26) at the desired SNR level, the noise-corrupted 230 data files are transformed into time-domain data files using IFFT. Following AGR processing to obtain t_p, f_p, α_p, and B_p, $p = 0, 1, 2, \ldots, p_{\max}$, the 2-D geometrical moments of these data files are computed using (17)–(19). The AGR processing is adjusted such that the iteration is stopped when the ratio γ exceeds at least 0.9 as in the previous case, resulting in $p_{\max} \leq 30$ for most aspect angles of the five targets.

To obtain feature vectors consisting of the computed geometrical moments, the maximum order $L = 10$ is used, yielding

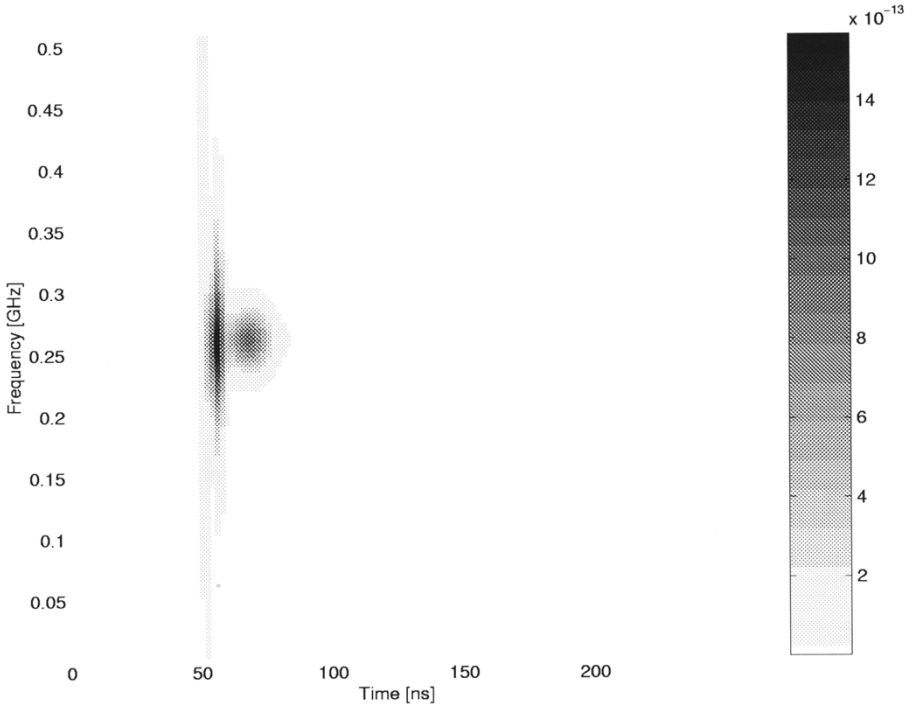

Fig. 7. ADS result of Target-4 (the AGR iteration continues until the γ exceeds at least 0.9, resulting in $p_{\max} = 13$).

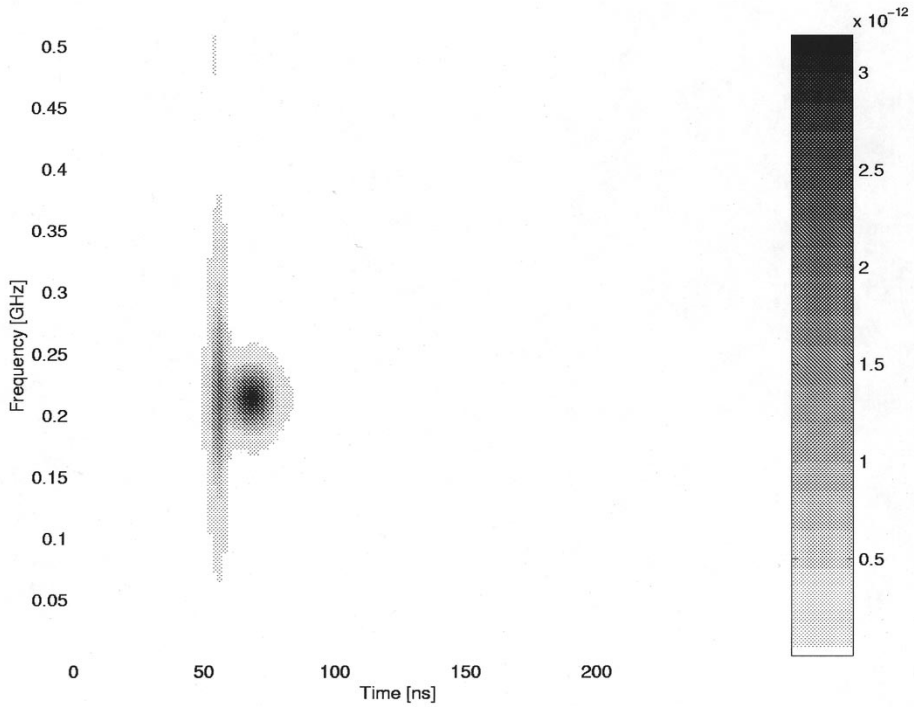

Fig. 8. ADS result of Target-5 (the AGR iteration continues until the γ exceeds at least 0.9, resulting in $p_{\max} = 10$).

$K = L \times 3 = 30$, which is the dimension of $\mathbf{x}$ in (20). Although the dimension $K = 30$ is reasonably small, we applied the PCA to further reduce $K = 30$ in order to reduce the computation burden of the classifier. Since $N_c = 5$ and $N_a = 46$, $\mathbf{X}$ in (21) is a 30×230 matrix. Instead of the eigen-decomposition of $\mathbf{R}_{\mathbf{xx}}$, the SVD is directly applied to $\mathbf{X}'$ for estimating the eigenvalues and eigenvectors of $\mathbf{R}_{\mathbf{xx}}$.

The distribution of the 30 eigenvalues of the covariance matrix $\mathbf{R}_{\mathbf{xx}}$, which is a 30×30 matrix in this case, is shown in Fig. 10. It shows a rapid decrease of the eigenvalues and the

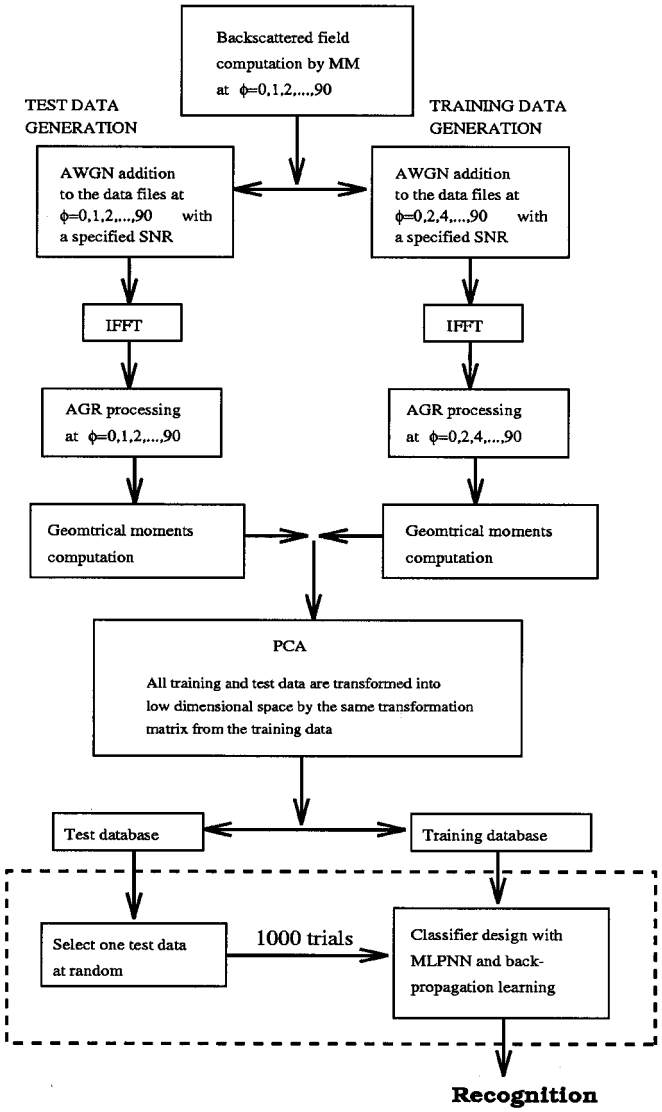

Fig. 9. The experimental setup for demonstrating the proposed technique.

eigenvalues larger than 7 are negligibly small. Therefore, the remaining 23 eigenvalues can be ignored to produce transformation matrix $\mathbf{P}$, yielding the final feature vector $\mathbf{y}$ of dimension 7. If the 127×127 ADS image is directly used for classification, the amount of memory storage for one feature vector is equal to $127^2 = 16\,129$. Hence, in terms of the amount of memory storage, a very large compression ratio of $16\,129/7 = 2304.1$ has been achieved through the combined use of geometrical moments and PCA in this study.

To understand the behavior of the feature vector $\mathbf{y}$ in the reduced feature space, the trajectories of $\mathbf{y}$ for the five targets are plotted in Fig. 11. For convenience, this figure shows the first three components of $\mathbf{y}$. The axes correspond to the three dominant eigenvectors of the covariance matrix $\mathbf{R}_{\mathbf{xx}}$, and the first component of $\mathbf{y}$ is equivalent to the projection value of $\mathbf{x}$ onto the first dominant eigenvector direction, etc. As shown in Fig. 11, different targets produce different trajectories as the aspect angle varies. For full 360° aspect data, the trajectory of each target would be closed. In Fig. 11, one can observe that the two trajectories of Target-3 and Target-4 are quite closer during all 46 aspects than other trajectories. In Table I, the physical dimensions of Target-3 and Target-4 are very similar in comparison with those of the other targets. This similarity causes the above closeness between the two trajectories.

With the obtained 230 training data $\mathbf{y}$, the MLPNN classifier in Fig. 2 is trained with the back propagation learning algorithm, and its weights connecting between neurons are determined. To obtain the best classification accuracy, the training iteration of the MLPNN is terminated when the MSE is less than 10^{-3} or the maximum epoch of 2000 is reached. Note that one complete presentation of the entire training set during the training process is called an epoch [25]. For testing this classifier, the data files from all azimuth angles at $\phi = 0^\circ, 1^\circ, 2^\circ, \ldots, 90^\circ$ are used, resulting in 5 (number of target classes) $\times$ 91 (number of azimuth angle settings) $= 455$ test data files. Note that the given test data set includes data files at odd aspect angles, which were not used for training, in addition to those at even aspect angles, which were used for training. Therefore, approximately half of the test data set was not used to design the classifier. Next, each data file is contaminated by independent AWGN to achieve the desired SNR. In this experiment, the SNR is varied from 0 dB to 40 dB with 5 dB steps for both training and testing. After the noise addition, 455 feature vectors $\mathbf{y}$ of dimension 7 are generated using the same procedure as for the training case. Note that the test feature vector $\mathbf{x}$, which consists of geometrical moments, is transformed into the lower dimensional feature vector $\mathbf{y}$ by the same transformation matrix $\mathbf{P}$ from the training data.

Finally, we have a test database containing 455 feature vectors for investigating the performance of the designed MLPNN classifier. From it, we randomly select one test feature vector $\mathbf{y}$ at a time. Thus, in this five-target classification experiment, each target has a 1/5 probability of being selected. The selected test feature vector is classified as one of the five target classes using the designed classifier. This selection and classification process is repeated 1000 times, and the correct classification rate P_c is estimated as

$$P_c = \frac{\text{Number of correct classifications}}{1000}. \tag{29}$$

To obtain more reliable results, 50 Monte Carlo simulations of the above 1000 test feature selection and classification experiment were performed to provide the estimates of the resultant sample averaged correct classification rate $P_{c,\,av}$, along with the sample standard deviation of the probability of correct estimate.

In addition to the five-target classification experiments, we also have performed a three-target classification experiment involving Target-1, Target-2, and Target-3. Since only three targets are used for classification, the number of data files for training is given by 3 (number of target classes) $\times$ 46 (number of even azimuth angle settings) $= 138$, and the number of test data files is 3 (number of target classes) $\times$ 91 (number of azimuth angle settings) $= 273$. We have followed the same procedure as in the previous five-target classification experiment, i.e., 50 Monte Carlo simulations were performed to estimate $P_{c,\,av}$.

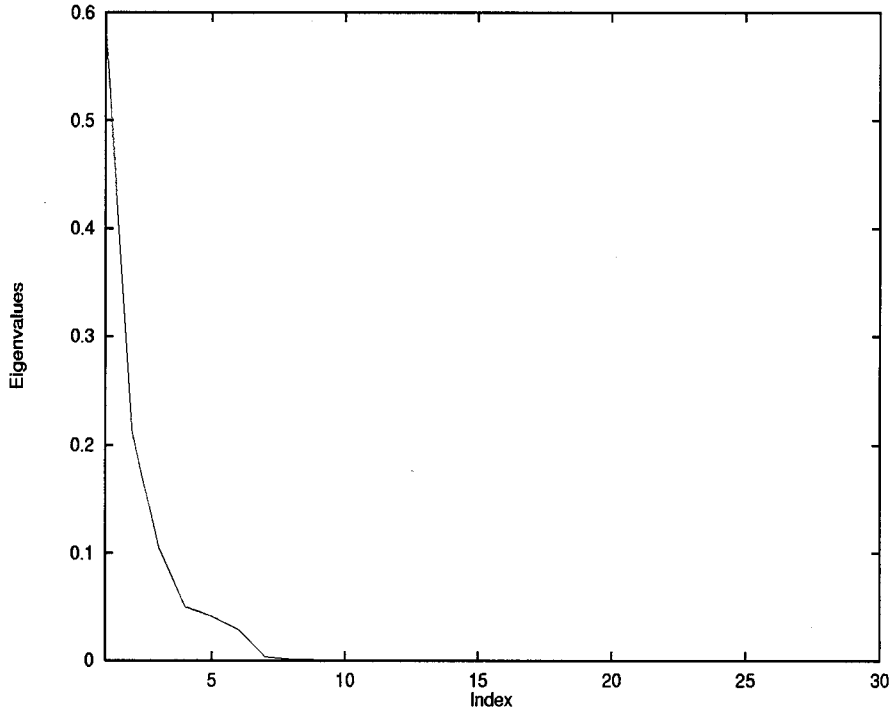

Fig. 10. The distribution of 30 eigenvalues of the covariance matrix.

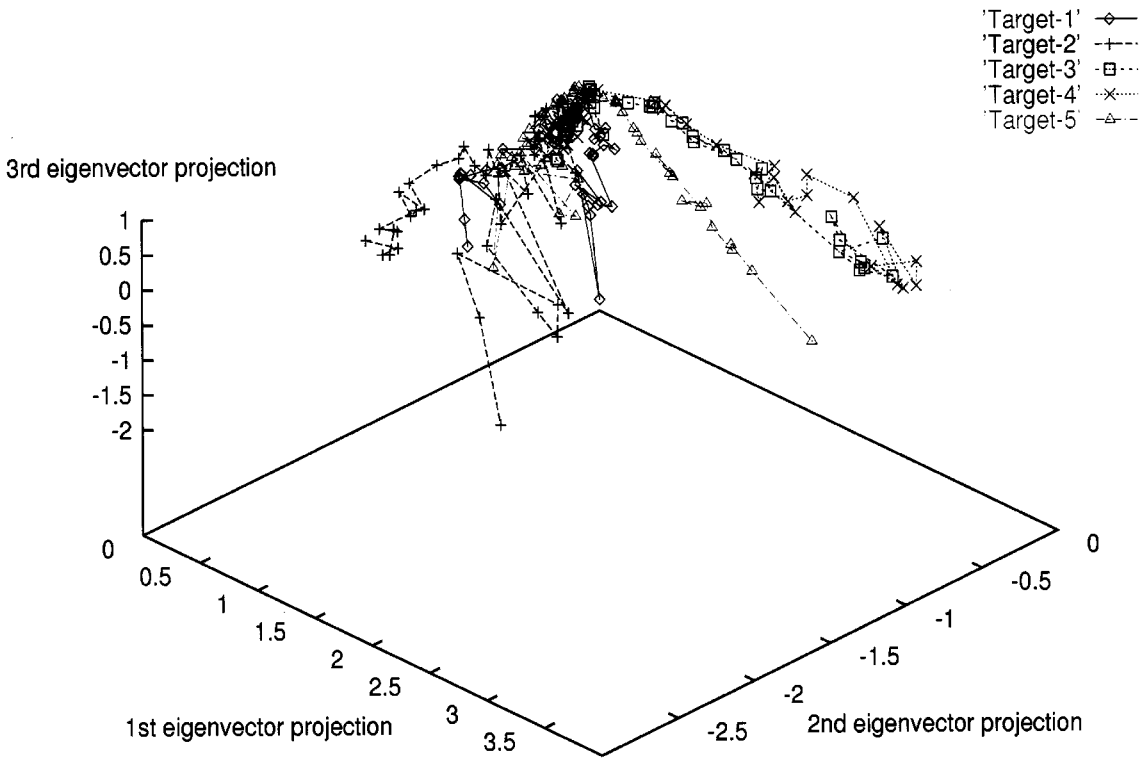

Fig. 11. Feature space trajectories for the five targets.

The results of classifications for the five-target and three-target experiments are shown in Figs. 12 and 13. These figures show how probability of correct classification varies as the SNR varies from 0 dB to 40 dB. The error bars around estimated $P_{c,\,av}$ values mark one (estimated) standard deviation above and below the estimated $P_{c,\,av}$ values. From Fig. 12, one can identify that the $P_{c,\,av}$ value for the five-target case achieves approximately 93% accuracy in the high SNR range between 25–40 dB, and it decreases rapidly at the SNR levels below 15 dB. For the three-target case in Fig. 13, the $P_{c,\,av}$

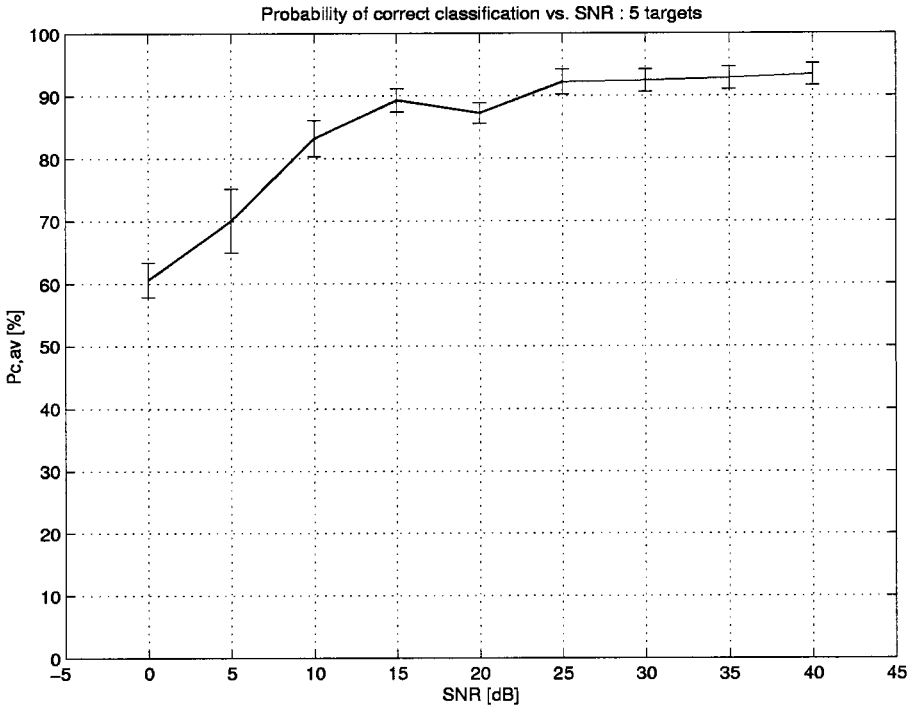

Fig. 12. The average values of correct estimates $P_{c,av}$ against SNR for the five-target classification experiments, 50 Monte Carlo simulations.

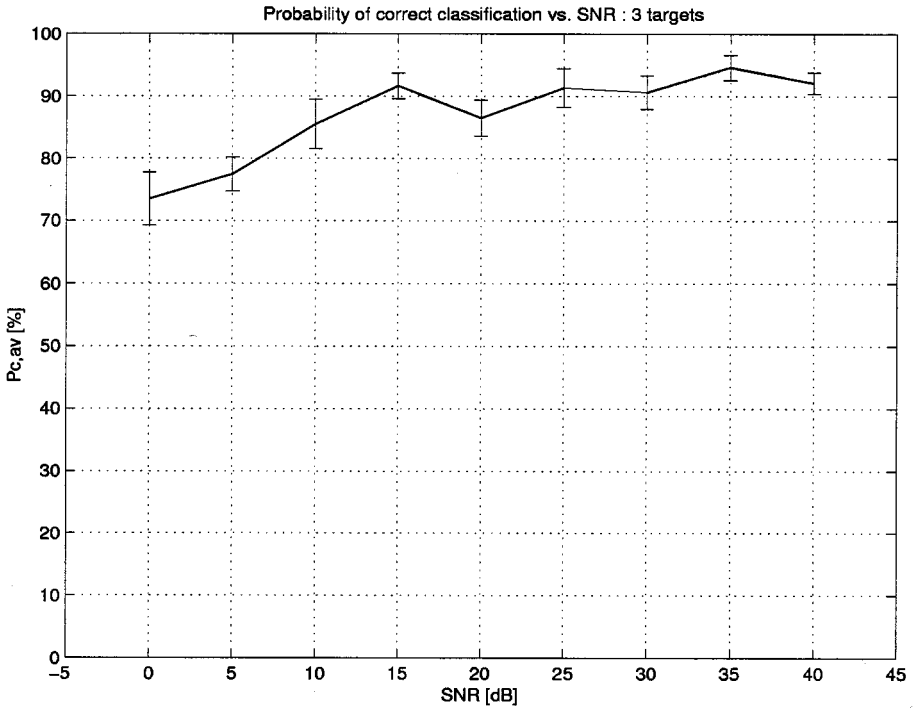

Fig. 13. The average values of correct estimates $P_{c,av}$ against SNR for the three-target classification experiments, 50 Monte Carlo simulations.

shows similar behavior in the SNR range between 15–40 dB, but as expected, it is higher in the low SNR range than that of the five-target case. From the results in Figs. 12 and 13, it can be seen that the proposed procedure for radar target recognition can provide successful classification performance even at SNR levels as low as 15 dB.

VII. Conclusion

In this paper, we have developed a new target recognition procedure based on AGR processing, which is an adaptive joint time-frequency processing technique. In order to efficiently obtain feature vectors for target recognition, the closed-form ex-

pressions of geometrical moments for ADS have been derived to provide efficient and accurate computation. After applying PCA to the computed geometrical moments, their dimensionality can be further reduced to a much smaller dimension, yielding a very large compression ratio. The resulting small dimensional feature vectors are identified using the well-known MLPNN classifier. The results show that the target recognition system based on the proposed scheme can give successful correct classification rates in the low SNR range with low computational costs.

ACKNOWLEDGMENT

The authors would like to acknowledge the help of J.-H. Lee, S.-J. Han, and D.-K. Seo.

REFERENCES

[1] D. L. Mensa, *High Resolution Radar Cross-Section Imaging* Norwood, MA: Artech House, 1991.
[2] E. C. Botha, E. Barnard, and C. J. Barnard, "Feature-based classification of aerospace radar targets using neural networks," *Neural Networks*, vol. 9, no. 1, pp. 129–142, 1996.
[3] E. Rothwell, D. P. Nyquist, K. M. Chen, and B. Drachman, "Radar target discrimination using the extinction-pulse technique," *IEEE Trans. Antennas Propagat.*, vol. 33, pp. 929–937, Sept. 1985.
[4] K. M. Chen, D. P. Nyquist, E. J. Rothwell, L. L. Webb, and B. Drachman, "Radar target discrimination by convolution of radar returns with extinction pulses and single-mode extraction signals," *IEEE Trans. Antennas Propagat.*, vol. 34, pp. 896–904, July 1986.
[5] J. E. Moony, Z. Ding, and L. S. Riggs, "Robust target identification in white Gaussian noise for ultra wide-band radar systems," *IEEE Trans. Antennas Propagat.*, vol. 46, pp. 1817–1823, Dec. 1998.
[6] A. Moghaddar and E. K. Walton, "Time-frequency distribution analysis of scattering from waveguide cavities," *IEEE Trans. Antennas Propagat.*, vol. 41, pp. 677–680, May 1993.
[7] L. C. Trintinalia and H. Ling, "Interpretation of scattering phenomenology in slotted waveguide structures via time-frequency processing," *IEEE Trans. Antennas Propagat.*, vol. 43, pp. 1253–1261, Nov. 1995.
[8] H. Kim and H. Ling, "Wavelet analysis of radar echo from finite-sized targets," *IEEE Trans. Antennas Propagat.*, vol. 41, pp. 200–207, Feb. 1993.
[9] S. Qian and D. Chen, "Signal representation using adaptive normalized Gaussian functions," *Signal Processing*, vol. 36, pp. 1–11, Mar. 1994.
[10] Q. Yin, Z. Ni, S. Qian, and D. Chen, "Adaptive oriented orthogonal projective decomposition" (in Chinese), *J. Electron.*, vol. 25, no. 4, pp. 52–58, Apr. 1997.
[11] S. Mallat and Z. Zhang, "Matching pursuit with time-frequency dictionaries," *IEEE Trans. Signal Processing*, vol. 41, pp. 3397–3415, Dec. 1993.
[12] L. C. Trintinalia and H. Ling, "Joint time-frequency ISAR using adaptive processing," *IEEE Trans. Antennas Propagat.*, vol. 45, pp. 221–227, Feb. 1997.
[13] L. C. Trintinalia, R. Bhalla, and H. Ling, "Scattering center parameterization of wide-angle backscattered data using adaptive Gaussian representation," *IEEE Trans. Antennas Propagat.*, vol. 45, pp. 1664–1668, Nov. 1997.
[14] Y. Wang, H. Ling, and V. C. Chen, "ISAR motion compensation via adaptive joint time-frequency processing," *IEEE Trans. Aerosp. Electron. Syst.*, vol. 34, pp. 676–679, Apr. 1998.
[15] S. Abrahamson, B. Brusmark, H. C. Strifors, and G. C. Gaunaurd, "Aspect dependence of time-frequency signatures of a complex target extracted by impulse radar," in *Proc. IEEE 1995 Int. Radar Conf.*, Alexandria, VA, May 1995, pp. 444–449.
[16] M. Bastiaans, "Gabor's expansion of a signal into Gaussian elementary signals," *Proc. IEEE*, vol. 68, pp. 538–539, Apr. 1980.
[17] T. L. Sarkar and C. Su, "A tutorial on wavelets from an electrical engineering perspective—Part 2: The continuous case," *IEEE Antennas Propagat. Mag.*, vol. 40, pp. 36–49, Dec. 1998.
[18] S. Qian and D. Chen, "Joint time-frequency analysis," *IEEE Signal Processing Mag.*, pp. 51–67, Mar. 1999.
[19] V. C. Chen and H. Ling, "Joint time-frequency analysis for radar signal and image processing," *IEEE Signal Processing Mag.*, pp. 81–93, Mar. 1999.
[20] M.-K. Hu, "Visual pattern recognition by moments invariants," *IRE Trans. Information Theory*, vol. 8, pp. 179–187, Feb. 1962.
[21] S. A. Dudani, K. J. Breeding, and R. B. McGhee, "Aircraft identification by moments invariants," *IEEE Trans. Comput.*, vol. 26, pp. 39–45, Jan. 1977.
[22] A. Khotanzad and J.-H. Lu, "Classification of invariant image representations using a neural network," *IEEE Trans. Acoust. Speech Signal Process.*, vol. 38, pp. 1028–1038, June 1990.
[23] A. Papoulis, *Probability, Random Variables, and Stochastic Processes*, 3rd ed. New York: McGraw-Hill, 1991.
[24] K.-T. Kim and H.-T. Kim, "One-dimensional scattering ceter extraction for efficient radar target classification," *IEE Proc. Radar, Sonar, Navigat.*, vol. 146, pp. 147–158, June 1999.
[25] S. Haykin, *Neural Networks*, 2nd ed. Englewood Cliffs, NJ: Prentice-Hall, 1999.

Kyung-Tae Kim was born in Taejon, Korea on April 15, 1970. He received the B.S., M.S., and Ph.D. degrees in electrical engineering from the Department of Electrical Engineering at the Pohang University of Science and Technology (POSTECH), Pohang, Kyungpook, Korea, in 1994, 1996, and 1999, respectively.

Since March 1999, he has been working at the Electromagnetics Technology Lab., POSTECH as a Research Engineer. His primary research interests include radar target imaging and recognition, super-resolution processing techniques, neural networks, and RCS measurement and prediction.

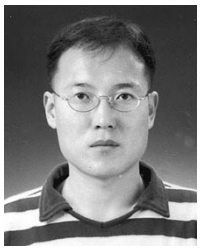

In-Sik Choi received the B.S. degree in electrical engineering from Kyungpook National University, Taegu, Korea in 1998 and the M.S. degree in electrical engineering from Pohang University of Science and Technology (POSTECH), Pohang, Korea in 2000. He is currently pursuing his Ph.D. degree in electrical engineering also at POSTECH.

His research areas include computational electromagnetics as well as signal processing with application to radar target identification.

Hyo-Tae Kim received the B.S. and M.S. degrees in electronics engineering from Seoul National University, Seoul, Korea, in 1978 and 1982, respectively, and the Ph.D. degree in electrical engineering from the Ohio State University, Columbus, OH in 1986.

After his graduate work at the ElectroScience Laboratory, the Ohio State University, he joined the faculty of POSTECH (Pohang University of Science and Technology), Pohang, Korea, where he is now a Professor. His research activity and interests are in the areas of antennas, EM scattering, EMI/EMC, and radar signal processing for imaging and identification.